J. Fluid Mech. (2000), *vol.* 415, *pp.* 45–64. Printed in the United Kingdom

A numerical study of the particle size distribution of an aerosol undergoing turbulent coagulation

By WALTER C. READE[1] AND LANCE R. COLLINS[2]†

[1]International Paper, 6285 Tri-Ridge Blvd., Loveland, OH 45140, USA

[2]Department of Chemical Engineering, The Pennsylvania State University, University Park, PA 16802, USA

(Received 23 November 1999 and in revised form 14 February 2000)

Coagulation and growth of aerosol particles subject to isotropic turbulence has been explored using direct numerical simulations. The computations follow the trajectories of 262 144 initial particles as they are convected by the turbulent flow field. Collision between two parent particles leads to the formation of a new daughter particle with the mass and momentum (but not necessarily the energy) of the parent particles. The initially monodisperse population of particles will develop a size distribution over time that is controlled by the collision dynamics. In an earlier study, Sundaram & Collins (1997) showed that collision rates in isotropic turbulence are controlled by two statistics: (i) the radial distribution of the particles and (ii) the relative velocity probability density function. Their study considered particles that rebound elastically; however, we find that the formula that they derived is equally valid in a coagulating system. However, coagulation alters the numerical values of these statistics from the values they attain for the elastic rebound case. This difference is substantial and must be taken into consideration to properly predict the evolution of the size distribution of a population of particles. The DNS results also show surprising trends in the relative breadth of the particle size distribution. First, in all cases, the standard deviation of the particle size distribution of particles with finite Stokes numbers is much larger than the standard deviation for either the zero-Stokes-number or infinite-Stokes-number limits. Secondly, for particles with small initial Stokes numbers, the standard deviation of the final particle size distribution decreases with increasing initial particle size; however, the opposite trend is observed for particles with slightly larger initial Stokes numbers. An explanation for these phenomena can be found by carefully examining the functional dependence of the radial distribution function on the particle size and Stokes number.

1. Introduction

The effect of turbulent coagulation on the evolution of the particle size distribution of an aerosol is not well understood, despite its importance in a broad range of technological and naturally occurring flows. Examples of flows where turbulent coagulation is likely to play an important role include such diverse topics as powder manufacturing (Pratsinis, Zhu & Vemury 1996; Moody & Collins 2000) soot formation in turbulent flames (Fairweather *et al.* 1992) and raindrop formation from cloud drop nuclei (Pinsky & Khain 1997; Shaw *et al.* 1998). In each example, turbulent fluctuations can induce relative motion between neighbouring particles or drops causing

† Author to whom correspondence should be addressed.

an enhancement of the collision rate. Moreover, because the dynamic response of each particle is a sensitive function of its size and response time, turbulent coagulation can bias collision statistics causing a substantial change in the shape of the particle size distribution.

Experimental observations of turbulent coagulation in the literature focus primarily on the evolution of the particle size distribution (Adachi, Stuart & Fokkink 1994; Yuu & Umekage 1996; Kusters, Wijers & Thoenes 1997). Due to limitations in the spatial and temporal resolution of most experiments, direct measurement of the collision rates between particle classes is not yet feasible. Furthermore, the time-dependent particle (drop) size distribution cannot be related to the underlying collision kernel without invoking *ad hoc* assumptions to make the so-called 'inverse problem' well posed (Rosner & Tassopoulos 1991). Consequently, the relationship between the turbulence parameters, particle properties and the associated collision kernel remains poorly understood.

Direct numerical simulation (DNS) has recently begun to fill the void by providing an accurate 'model-free' representation of dilute turbulent aerosols. Early studies focused on point-mass (collision-free) particles (Elghobashi 1991; Elghobashi & Truesdell 1992; McLaughlin 1994). An important finding of the early work is that particle concentrations in a turbulent flow field can become highly inhomogeneous (Maxey 1987; Squires & Eaton 1991; Wang & Maxey 1993) when particle response times are of the order of the Kolmogorov time scale. This effect results from local regions of strong vorticity acting like centrifuges, forcing particles out of vortex cores and into the high-strain regions that lie in between. As a consequence, local concentrations of particles can be much higher than the average concentration. This phenomenon, often referred to as 'preferential concentration', has been observed in experiments as well (Eaton & Fessler 1994). The effect that preferential concentration has on collision rates of finite-size particles was investigated by Sundaram & Collins (1997). They found collision enhancements as large as 1–2 orders of magnitude for particles with response times near the Kolmogorov time scale, as have other more recent investigations (Zhou, Wexler & Wang 1998; Chen, Kontomaris & McLaughlin 1998).

The focus of the present study is on how turbulent coagulation affects the particle size distribution of an initially monodisperse population of particles. We are concerned with particle loadings that are dilute, and so we ignore the effect of the particles on the fluid motion (so-called reverse coupling). This corresponds to the asymptotic limit of zero particle loading. Of course, the simulations have a finite particle loading; however, we are careful to remain in the regime of small mass loadings (see Sundaram & Collins 1999 for an in-depth discussion of this point). The simulations are similar to earlier ones of elastically rebounding particles by Sundaram & Collins (1997); however, in the present simulations, particle collisions lead to coagulation events. Particle populations are then monitored for arbitrary periods of time to determine how the particle size distribution evolves. The goal of this investigation is to understand how particle and turbulence properties affect the particle size distribution. We also compare the results from the simulations to limiting solutions for particles with zero response time (Saffman & Turner 1956; Wang, Wexler & Zhou 1998*a*; Brunk, Koch & Lion 1997, 1998*a*, *b*) and infinite response time (Abrahamson 1975; Reade & Collins 1998).

The paper is organized as follows. Section 2 gives an overview of the governing equations and the numerical methods used to solve them. The major findings of the study are then presented in § 3, followed by conclusions in § 4.

2. Governing equations

The domain of the simulations consists of a periodic cube of fluid of length 2π (in arbitrary units). By periodic we mean that fluid or particles that leave one bounding surface of the cube immediately enter the opposite bounding surface. Thus, the total mass in the cube is conserved. To simplify the analysis of the results, the turbulence is made statistically stationary by introducing large-scale forcing. This eliminates the complication of time-dependent turbulence length and time scales. The governing equations and numerical algorithms used to solve them are summarized below.

2.1. *Fluid mechanics*

We assume that the flow is incompressible and isothermal. Furthermore, we neglect the effect of the suspended particles on the flow under the assumption of dilute conditions. Consequently, the equations governing the velocity field and pressure are

$$\nabla \cdot \boldsymbol{u} = 0, \tag{2.1}$$

$$\frac{\partial \boldsymbol{u}}{\partial t} + \boldsymbol{u} \cdot \nabla \boldsymbol{u} = -\frac{\nabla p}{\rho} + \nu \nabla^2 \boldsymbol{u} + \boldsymbol{F}, \tag{2.2}$$

where $\boldsymbol{u}$ is the local fluid velocity, p is the pressure, ρ is the fluid density, ν is the kinematic viscosity and $\boldsymbol{F}$ is a solenoidal forcing function. We use a forcing scheme similar to the one described by Eswaran & Pope (1988).

The velocity field is updated in Fourier space using a pseudospectral algorithm (Canuto *et al.* 1988). The time update of the Fourier amplitudes is accomplished using a fourth-order Runge–Kutta method.

2.2. *Aerosol particles*

The trajectory of each particle is computed based on the analysis of Maxey & Riley (1983). If the density of the particles is much larger than the carrier gas (typically we expect $\rho_p/\rho = O(100\text{–}1000)$, where ρ_p is the particle density), the equations reduce to

$$\frac{\mathrm{d}\boldsymbol{x}_p^{(i)}}{\mathrm{d}t} = \boldsymbol{v}_p^{(i)}, \tag{2.3}$$

$$\frac{\mathrm{d}\boldsymbol{v}_p^{(i)}}{\mathrm{d}t} = \frac{\boldsymbol{u}(\boldsymbol{x}_p^{(i)}) - \boldsymbol{v}_p^{(i)}}{\tau_p^{(i)}} + \frac{1}{m_p^{(i)}} \sum_{j \neq i} \boldsymbol{F}^{(ij)}, \tag{2.4}$$

where $\boldsymbol{x}_p^{(i)}$ and $\boldsymbol{v}_p^{(i)}$ are the position and velocity of the centroid of the ith particle, $a^{(i)}$, $m_p^{(i)}$ and $\tau_p^{(i)} \equiv (\rho_p/\rho)(a^{(i)})^2/(9\nu)$ are the radius, mass and response time of the ith particle, and $\boldsymbol{F}^{(ij)}$ is the impulsive force experience by the ith particle due to a collision with the jth particle. A similar equation can be written and integrated for each particle in the system.

The numerical algorithm used to update the position and velocity of each of the particles must also check for possible collisions between particles. Owing to the large number of possible colliding *pairs* in the system, a neighbourhood searching algorithm, similar to the one described in Sundaram & Collins (1996), is used. We define the collision time, $\Delta t^{(ij)}$, as the time for particles i and j to make contact. Each pair of particles that satisfies $0 \leqslant \Delta t^{(ij)} \leqslant \Delta t$ is added to the collision list. The collision list is sorted in order of increasing $\Delta t^{(ij)}$, and then each collision is enacted in turn. Collisions are assumed to produce a coagulation event with 100% efficiency, yielding a spherical daughter particle with the following properties (note that variables with a

U'	ϵ	ν	ρ	L	T	η	τ_η	Re	$k_{max}\eta$
0.84	0.20	1.3×10^{-2}	1.0	1.65	1.98	5.6×10^{-2}	0.25	54.5	1.8

TABLE 1. Summary of turbulence conditions for all of the simulations (in arbitrary units, with the exception of the final two terms which are dimensionless). U' is the turbulence intensity, ϵ is the dissipation rate, ν is the kinematic viscosity, ρ is the density, L is the integral length scale, T is the large-eddy turnover time, η is the Kolmogorov length scale, τ_η is the Kolmogorov time scale, Re is the Reynolds number (based on the Taylor microscale), and $k_{max}\eta$ is a measure of the fine-scale resolution of the simulation.

prime refer to properties of the daughter particle):

$$m'^{(i)}_p = m^{(i)}_p + m^{(j)}_p, \tag{2.5}$$

$$\boldsymbol{v}'^{(i)}_p = \frac{m^{(i)}_p \boldsymbol{v}^{(i)}_p + m^{(j)}_p \boldsymbol{v}^{(j)}_p}{m'^{(i)}_p}, \tag{2.6}$$

where we assume that $i < j$ and for accounting purposes assign the daughter particle to the smaller index, i (the jth particle is removed from the system). Following each collision update, the remaining pairs are again checked and re-sorted to ensure that the newly-formed daughter particle does not change the outcome of the remaining collisions. This process is continued until all of the colliding pairs in the list have been updated.

The positions and velocities of the remaining (non-colliding) particles are then advanced using a fourth-order Runge–Kutta algorithm with an exact treatment of the linear terms (we use an integrating factor in the update). Fluid velocities are interpolated to particle centres using a fourth-order Hermite polynomial approximation.

2.3. *Parameters*

Isotropic turbulent flow is characterized by three parameters: the turbulence intensity, U', the dissipation rate, ϵ, and the kinematic viscosity, ν, or equivalently one dimensionless parameter, the Reynolds number. Here we choose the Reynolds number based on the Taylor microscale, defined as

$$Re = \sqrt{\frac{15}{\nu\epsilon}} U'^2. \tag{2.7}$$

In general, this quantity is limited by the number of nodes used in the simulation. In this study we use 64^3 nodes for all of the runs, corresponding to $Re = 54$. The fluid properties are fixed throughout the entire study. A summary of the fluid parameters is given in table 1.

The introduction of an initially monodisperse population of particles into the system adds three more parameters: the particle density, ρ_p, the number of 'monomers', N_1, and the monomer radius, a_1. Note that superscripts refer to particle numbers whereas subscripts refer to particle 'categories'. For example at $t = 0$, the particles all belong to the monomer category, and so $a^{(i)} = a_1$ for $i = 1, ..., N_1$. The three variables that characterize the particle phase can be expressed in dimensionless form as

$$\phi \equiv \frac{4\pi a_1^3 N_1}{3V}, \tag{2.8}$$

Run	a_1	ρ_p	N_1	St_1	λ_1	ϕ
1	4.9×10^{-3}	122	64^3	0.2	0.0875	5.2×10^{-4}
2	4.9×10^{-3}	183	64^3	0.3	0.0875	5.2×10^{-4}
3	4.9×10^{-3}	305	64^3	0.5	0.0875	5.2×10^{-4}
4	4.9×10^{-3}	427	64^3	0.7	0.0875	5.2×10^{-4}
5	2.45×10^{-3}	487	64^3	0.2	0.04375	6.5×10^{-5}
6	9.8×10^{-3}	30	64^3	0.2	0.175	4.2×10^{-3}
7	2.45×10^{-3}	170	64^3	0.7	0.04375	6.5×10^{-5}
8	9.8×10^{-3}	107	64^3	0.7	0.175	4.2×10^{-3}

TABLE 2. Summary of initial aerosol properties for the eight simulations performed in this study. a_1 is the monomer radius, ρ_p is the particle density, N_1 is the initial number of monomers, St_1 is the monomer Stokes number, λ_1 is the monomer size parameter (made dimensionless by the Kolmogorov length scale, η), and ϕ is the volume fraction of particles.

$$\lambda_1 \equiv \frac{a_1}{\eta}, \tag{2.9}$$

$$St_1 \equiv \frac{2}{9}\left(\frac{\rho_p}{\rho}\right)\frac{{a_1}^2/\nu}{\sqrt{\nu/\epsilon}} = \frac{2}{9}\left(\frac{\rho_p}{\rho}\right){\lambda_1}^2, \tag{2.10}$$

where ϕ is the volume fraction of particles, $V \equiv (2\pi)^3$ is the volume of the box, λ_1 is a size parameter defined in terms of the Kolmogorov length scale, $\eta \equiv (\nu^3/\epsilon)^{1/4}$, and St_1 is the Stokes number, which is a dimensionless particle response time defined in terms of the Kolmogorov time scale, $(\nu/\epsilon)^{1/2}$. The parameters given in (2.7)–(2.10) define the initial state of the simulations.

3. Results and discussion

The specific runs performed in this study are summarized in table 2. In general, we focused on the effect of the initial Stokes number, St_1, and the initial particle size parameter, λ_1. In each case, an initially monodisperse population of particles is first allowed to equilibrate with the turbulence for eight large-eddy turnover times before coagulation is initiated. During this equilibration period, particle collisions are treated as hard-sphere elastic collisions. After eight large-eddy turnover times, coagulation is initiated and the particle size distribution is monitored until 25% of the particles have coagulated. Because of the different coagulation rates associated with each parameter set, the time required to complete each run varies substantially. However, comparisons are done at fixed percent coagulation so that intrinsic differences in the coagulation kernel can be separated from extrinsic differences in the rates of evolution of each system. Statistics of the particle and fluid phases are monitored at 5% intervals.

3.1. *Particle size distribution*

For an homogeneous system, it is possible to write a population balance for the evolution of n_i, defined as the number density of i-mers (e.g. $n_1 = N_1/V$, where V is the volume of the system). Following Smoluchowski (1917) we have

$$\frac{\mathrm{d}n_i}{\mathrm{d}t} = \frac{1}{2}\sum_{j=1}^{i-1} K_{i-j,j}\, n_{i-j} n_j - n_i \sum_{j=1}^{\infty} K_{i,j} n_j, \tag{3.1}$$

where $K_{i,j}$ is the collision kernel for collisions between i-mers and j-mers. The first term on the right-hand side accounts for additions to the i-mers due to collisions of smaller particles that produce an i-mer while the second term accounts for losses from this category due to collisions of an i-mer with anything. In principle, knowledge of the collision kernels allows the particle size distribution to be computed from (3.1). Sundaram & Collins (1997) derived the following generalized collision kernel for spherical particles suspended in a turbulent flow field:

$$K_{i,j} = 4\pi {a_{ij}}^2 g_{ij}(a_{ij}) \int_{-\infty}^{0} -w_{ij} P_{ij}(a_{ij}|w_{ij})\, \mathrm{d}w_{ij}, \tag{3.2}$$

where $a_{ij} \equiv (i^{1/3} + j^{1/3})a_1$ is the collision diameter, $g_{ij}(r)$ is the two-particle radial distribution function (hereafter referred to as the r.d.f.), $w_{ij} \equiv (\boldsymbol{v}_i - \boldsymbol{v}_j) \cdot (\boldsymbol{x}_i - \boldsymbol{x}_j)$ is the relative velocity along the line of centres, and $P_{ij}(r|w_{ij})$ is the relative velocity p.d.f. (probability density function) conditioned on the separation distance, r. (Note that (3.2) is a generalization of Sundaram & Collins 1997 for an arbitrary collision between an i-mer and a j-mer. In addition, the relative velocity integral is rewritten in accordance with the correction by Wang, Wexler & Zhou 1998*b*.) The above relationship is not a closed expression for the collision kernel, as $g_{ij}(r)$ and $P_{ij}(r|w_{ij})$ are not easily expressed in terms of the turbulence and particle parameters; nevertheless, (3.2) provides a framework for examining the results of the DNS, as will be shown.

Under two limiting conditions it is possible to determine $K_{i,j}$. If we consider $St_1 \ll 1$, the classical result of Saffman & Turner (1956) applies, and we can write

$$K_{i,j} = \left(\frac{8\pi}{15}\right)^{1/2} \left(\frac{\epsilon}{\nu}\right)^{1/2} a_{ij}^3. \tag{3.3}$$

Although some questions remain concerning the numerical coefficient in (3.3) (Brunk *et al.* 1997, 1998*a*, *b*; Wang *et al.* 1998*a*), there is general agreement on the functional form of $K_{i,j}$, which ultimately is what controls the shape of the particle size distribution.

In the other limit, $St_1 \gg 1$, kinetic theory applies and the collision rate can be expressed as (Abrahamson 1975)

$$K_{i,j} = \left[\frac{32\pi}{3}\left(\frac{E_i + E_j}{2}\right)\right]^{1/2} a_{ij}^2, \tag{3.4}$$

where E_i is the average kinetic energy (per unit mass) of the i-mers. In general, E_i is not known and must be solved for simultaneously. An analytical equation for E_i was derived by Reade & Collins (1998) based on the assumption of Gaussian velocity fluctuations. The resulting expression is

$$\frac{\mathrm{d}(n_i E_i)}{\mathrm{d}t} = \frac{1}{6}\sum_{j=1}^{i-1} K_{j,i-j} n_j n_{i-j} \Phi_{j,i-j} - \frac{7}{6} E_i n_i \sum_{j=1}^{\infty} K_{i,j} n_j - \frac{n_i(E_i - E_i^{eq})}{\tau_{p_i}}, \tag{3.5}$$

where

$$\Phi_{i,j} = \frac{(M_i E_i - M_j E_j)^2}{(E_i + E_j)} + 3(M_i^2 E_i + M_j^2 E_j), \tag{3.6}$$

$$M_i = \frac{i}{(i+j)}, \tag{3.7}$$

and E_i^{eq} is the equilibrium kinetic energy of the i-mers in the surrounding turbulence.

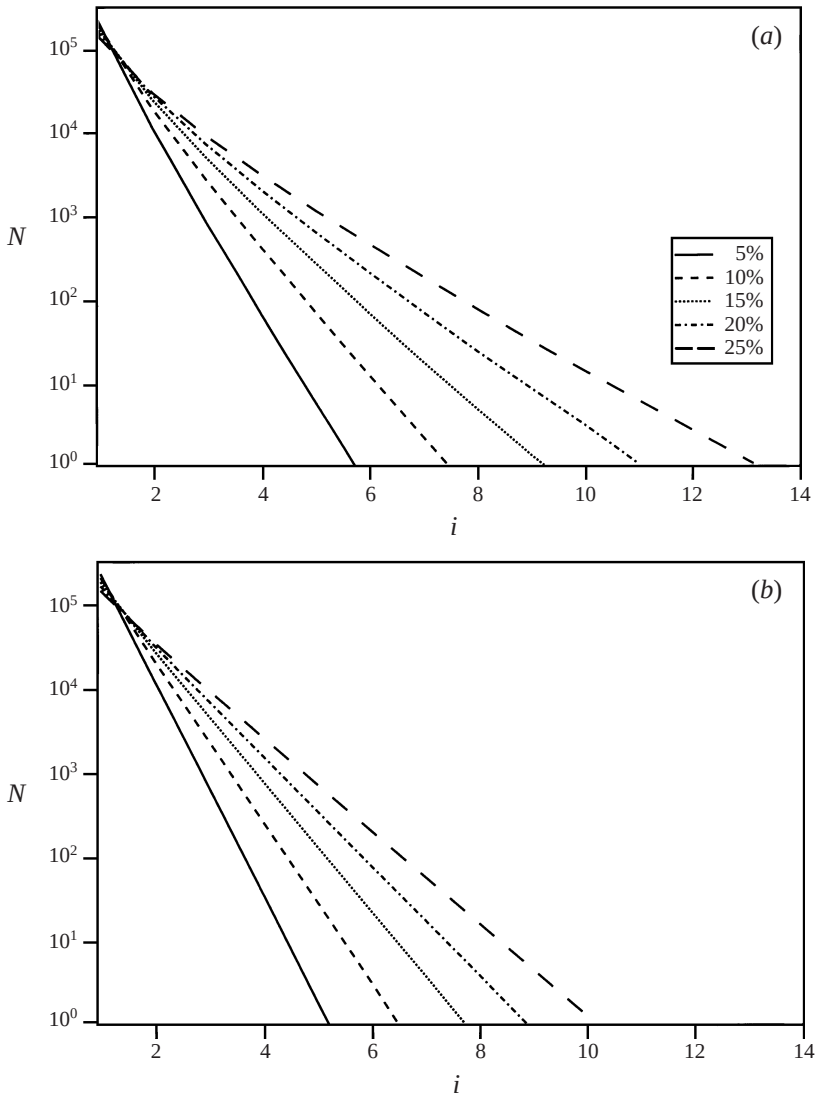

FIGURE 1. Particle size distributions for limiting cases of (*a*) zero Stokes number and (*b*) infinite Stokes number at 5% – 25% coagulation.

Recall that we are interested in the limit $\tau_{p_i} \to \infty$, thus the last term on the right-hand side of (3.5) represents an $O(St_1^{-1})$ correction. In the results presented below, we have neglected this term. Figure 1 shows the particle size distributions for the two limiting solutions at 5%, 10%, 15%, 20% and 25% coagulation. Notice that the Saffman & Turner kernel produces a broader distribution than the infinite-St kernel. This is due to the higher power of a_{ij} in (3.3) as compared to (3.4). This causes each subsequent generation to collide at a higher rate, accelerating the broadening of the distribution.

The size distribution of particles with finite initial Stokes number has been determined from the numerical simulations. The dependence of the distribution on the initial Stokes number, St_1, for fixed $\lambda_1 = 0.0875$ is shown in figure 2. First, it is apparent that the distributions for all of the finite-Stokes-number particles is much

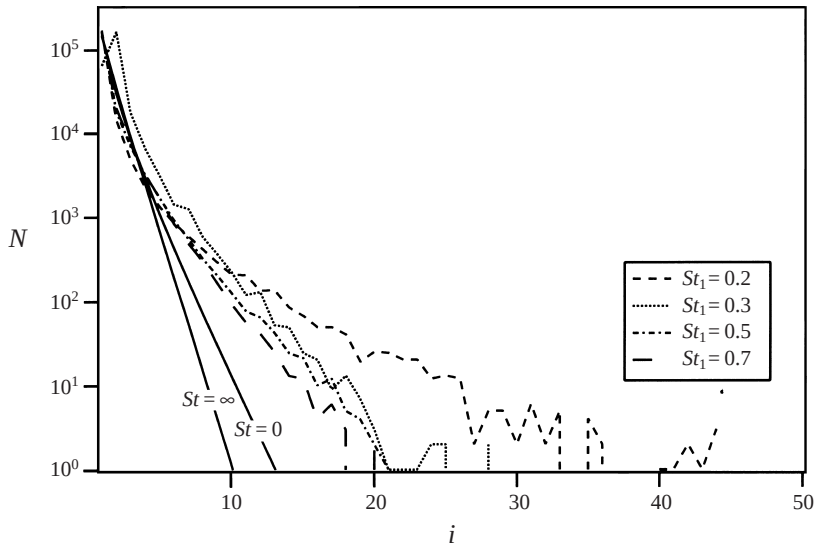

FIGURE 2. Particle size distribution from DNS at 25% coagulation for $\lambda_1 = 0.0875$ and for $St_1 = 0.2, 0.3, 0.5$ and 0.7. Solid lines show limiting solutions for zero and infinite Stokes numbers as indicated.

	5%	10%	15%	20%	25%
$St_1 = 0.2$	0.0733	0.1917	0.3690	0.7135	1.4504
$St_1 = 0.3$	0.0753	0.1972	0.3733	0.6130	0.8212
$St_1 = 0.5$	0.0753	0.1902	0.3399	0.5338	0.7766
$St_1 = 0.7$	0.0744	0.1790	0.3174	0.4856	0.6857
$p = 2$	0.0544	0.1145	0.1846	0.2608	0.3523
$p = 3$	0.0511	0.1221	0.2040	0.3502	0.4311
$p = 4$	0.0562	0.1272	0.2178	0.3347	0.4878
$p = 5$	0.0575	0.1336	0.2359	0.3762	0.5728
$p = 6$	0.0590	0.1418	0.2614	0.4411	0.7281
$p = 7$	0.0609	0.1529	0.3019	0.5746	1.2168
$p = 8$	0.0633	0.1700	0.3912	0.9773	1.6780

TABLE 3. Standard deviation of the particle size distributions shown in figure 2, normalized by the mean particle size, for $\lambda_1 = 0.0875$, as a function of Stokes number and percent coagulation. Also included for reference are standard deviations for the algebraic collision kernel proposed in (3.8) for $2 \leqslant p \leqslant 8$.

broader than either of the limiting solutions. Clearly, the dynamics of finite-inertia particles are not well represented by either limit. Furthermore, there is a noticeable trend that as St_1 increases, the breadth of the distribution decreases. This can be seen more quantitatively in table 3, which gives the standard deviation of each run at different percentages of coagulation. The standard deviation achieves the largest value for $St_1 = 0.2$ and the smallest for $St_1 = 0.7$.

It is tempting to try and at least correlate the DNS results by considering a collision kernel of the form

$$K_{i,j} = C a_{ij}^p, \tag{3.8}$$

where C and p are fitting parameters. In particular, by adjusting the power p it

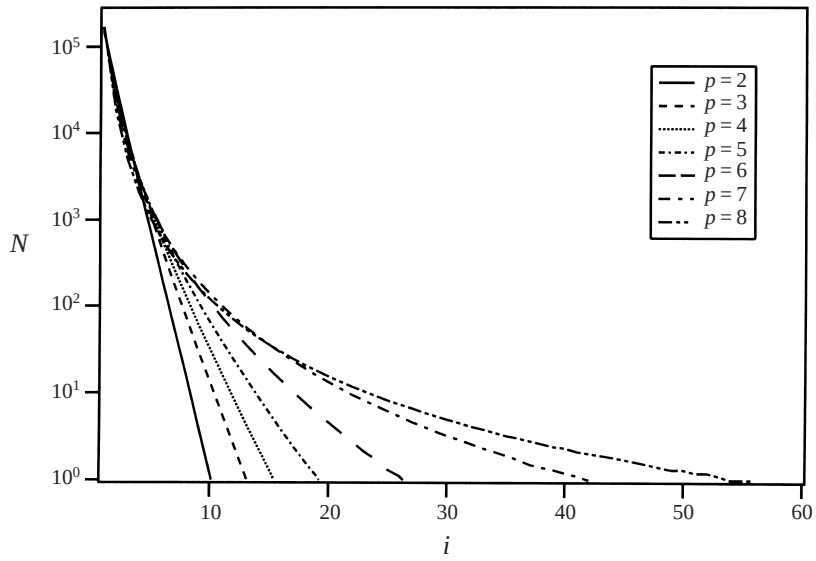

FIGURE 3. Particle size distribution for the power-law collision kernel given in (3.8) at 25% coagulation.

St_1	λ_1	5%	10%	15%	20%	25%
0.2	0.04375	0.0766	0.2140	0.4193	0.8836	—
0.2	0.0875	0.0753	0.1972	0.3690	0.7135	1.4504
0.2	0.175	0.0637	0.1614	0.3057	0.6231	0.7050
0.7	0.04375	0.0669	0.1518	0.2621	0.3935	0.5545
0.7	0.0875	0.0744	0.1790	0.3174	0.4856	0.6857
0.7	0.175	0.0689	0.1906	0.3646	0.6231	1.0905

TABLE 4. Standard deviation of the particle size distributions shown in figure 4, normalized by the mean particle size, as a function of Stokes number, size parameter and percent coagulation. The case of $St_1 = 0.2$, $\lambda_1 = 0.04375$ and 25% coagulation is not shown because the run was prohibitively long.

is possible to control the breadth of the distribution (or equivalently its standard deviation). Figure 3 shows particle size distributions that result from substituting (3.8) into (3.1) using $2 \leqslant p \leqslant 8$. Table 3 also summarizes the resulting standard deviations. It is apparent that no power, p, can effectively correlate the DNS results for all time. For example, to fit the $St_1 = 0.2$ case, the power p must be larger than 8 to get the 5% and 10% values, but it drops between 7 and 8 for the remaining percent coagulation. Thus, its value should be viewed as a dynamic quantity. Furthermore, the value of p required to correlate any of the finite-Stokes-number particles is much greater than either of the two limiting powers (i.e. $p = 3$ and $p = 2$ respectively). Clearly, something about the dynamics of real particles introduces new biases in the collision kernel that are not well represented by (3.3), (3.4) or (3.8). In § 3.4, we return to the question of the mechanism(s) responsible for broadening the particle size distribution of finite-Stokes-number particles.

Figure 4(*a*) shows the dependence of the particle size distribution on the initial size parameter, λ_1, at $St_1 = 0.2$. To accomplish this, the particle size and density are

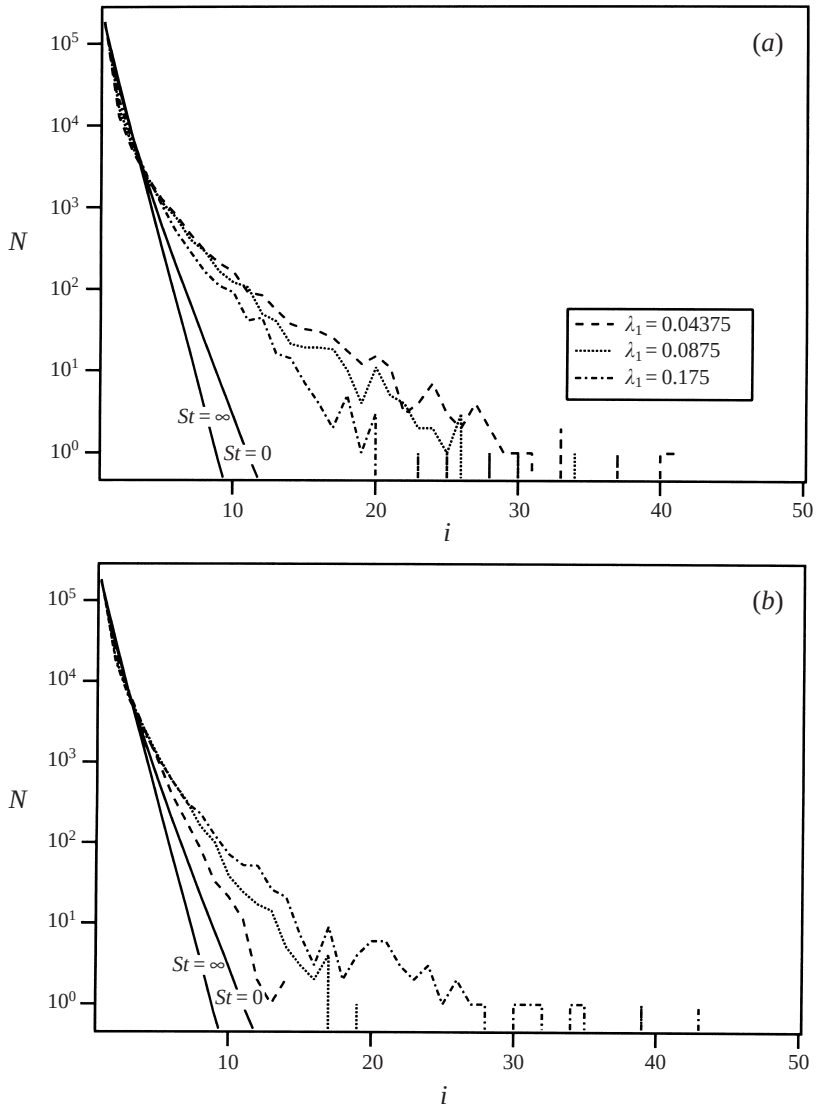

FIGURE 4. Particle size distribution from DNS for (*a*) $St_1 = 0.2$ and (*b*) $St_1 = 0.7$ and size parameters as indicated at 20% coagulation.

varied simultaneously such that $\rho_p a_1^2$ is constant. Notice that the broadest distribution occurs with the smallest initial particle and that the breadth *decreases* with increasing particle size. Quantitative results for the standard deviation, summarized in table 4, confirm these observations. The equivalent plot at $St_1 = 0.7$ is shown in figure 4(*b*). Remarkably, the trend in this case is reversed. That is, the narrowest distribution occurs with the smallest-sized particle, and the breadth *increases* with increasing particle size.

In order to explain these trends in the size distibutions, it is necessary to look more closely at the behaviour of the two underlying statistics that control the collision kernel, namely the r.d.f., $g_{ij}(r)$ and the relative velocity p.d.f., $P_{ij}(r|w_{ij})$. One complication associated with a coagulating system is the large matrix of interactions

that occur. For example, a system with K particle size categories has $K^2/2$ interactions. We cannot consider all of the interactions, due to the lack of adequate statistical samples; however, it is possible to consider a few low-order interactions and generalize the results to explain the trends observed in figures 2 and 4.

3.2. *Radial distribution function*

According to (3.2), the collision kernel is proportional to the r.d.f. at contact, $g_{ij}(a_{ij})$. It is therefore useful to consider the dynamics of this function as the coagulation process proceeds. For that purpose, it is convenient to define a residual radial distribution function (r.r.d.f.) as

$$h_{ij}(r) \equiv g_{ij}(r) - 1, \tag{3.9}$$

such that under the circumstance of a uniform distribution we expect that $h_{ij}(r) \approx 0$.

Figure 5 shows the r.r.d.f.s for (*a*) $h_{11}(r/a_{11})$; (*b*) $h_{22}(r/a_{22})$; and (*c*) $h_{12}(r/a_{12})$ at 5% and 25% coagulation for particles with an initial Stokes number, $St_1 = 0.7$, and initial size parameter, $\lambda_1 = 0.0875$. The abscissas are all normalized by the appropriate collision diameter so that contact corresponds to unity on each plot. Included in each graph is a curve corresponding to purely elastic collision with no coagulation (solid line) and a curve corresponding to interpenetrating or ghost particles (i.e. no interaction; dashed line). Notice that for all cases shown in figure 5(*a*), $h_{11}(1)$ is much larger than zero, indicating that preferential concentration is significantly enhancing the monomer–monomer collision rate. However, a comparison between the coagulation and elastic rebound cases shows that the latter has a much larger value at contact (by nearly an order of magnitude). The difference highlights the importance of the boundary condition at contact on the evolution of the r.d.f. In the coagulation case, two monomers at contact produce a dimer, thus lowering the concentration of monomers at small separations. This reduces the coagulating h_{11} distribution function at small separation distances.

The r.r.d.f. curves for the dimer–dimer interaction are given in figure 5(*b*). The larger scatter in these curves reflects the smaller statistical sample that is available. Nevertheless, it is readily apparent that the r.r.d.f. for the coagulating system at 5% coagulation is much greater than all of the other cases (including the elastic rebound case), whereas the curve for 25% coagulation is slightly below the elastic rebound case. The most likely explanation is that dimers initially form in the spatial vicinity of the parent monomers, hence at short times they have an r.r.d.f. that is similar to the monomer r.r.d.f. As time passes, the dimer r.r.d.f. eventually relaxes into equilibrium and looks closer to the elastic rebound case (actually a little below for the same reason that the coagulating r.r.d.f. for the monomer is reduced).

A result similar to that of the dimer–dimer r.r.d.f. is observed for the cross-correlation, $h_{12}(r/a_{12})$. The relatively high value at 5% coagulation again reflects a temporary disequilibrium that fades away with time. Also notice that the numerical value of the cross-correlation r.r.d.f. is smaller than either autocorrelation. This results from a suppression of the off-diagonal correlations due to slight mismatches in the local concentration of particles with different response times. As a result, particles are more likely to see other particles from their own size category than from other size categories. Reade & Collins (2000*b*) have explored this phenomenon and have shown that this 'diagonalization' of the collision kernel leads to a significant broadening of the particle size distribution.

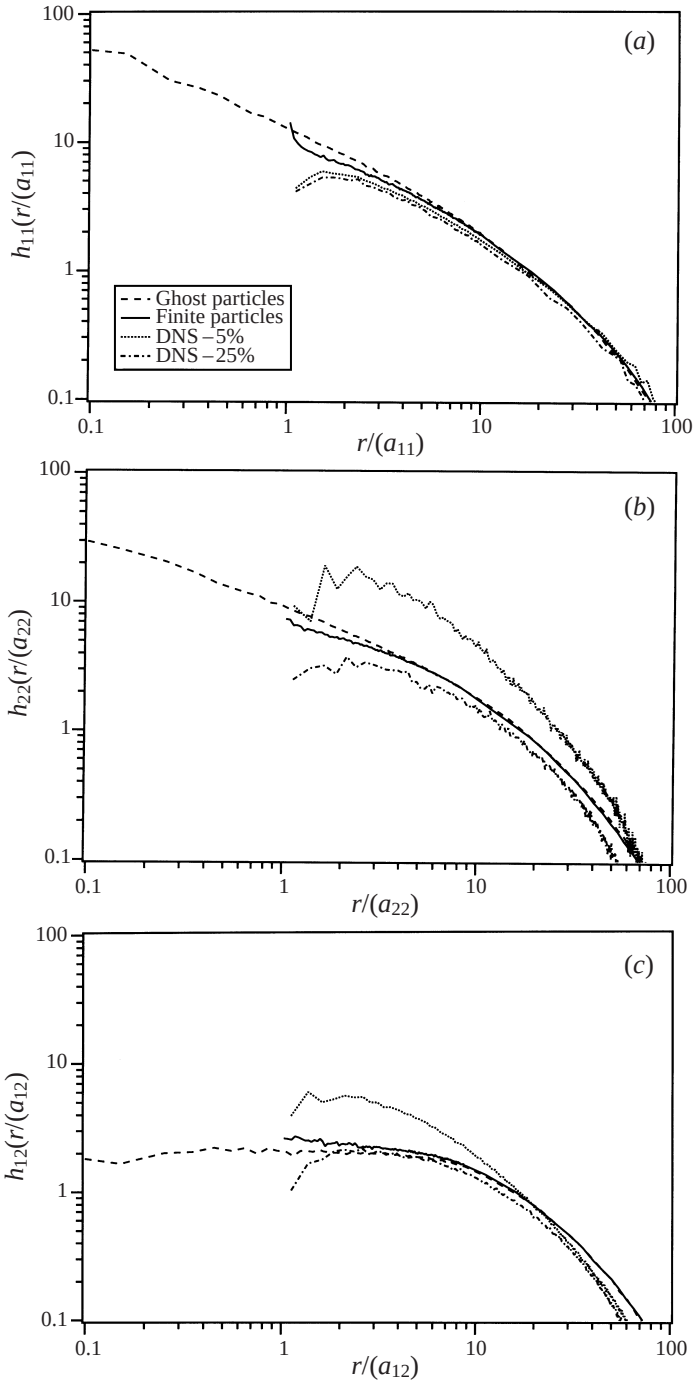

FIGURE 5. Residual radial distribution functions: (*a*) $h_{11}(r/a_{11})$, (*b*) $h_{22}(r/(a_{22}))$, and (*c*) $h_{12}(r/(a_{12}))$ for rebounding particles, ghost particles and for coagulating particles at 5% and 25% coagulation.

3.3. *Relative velocity statistics*

The second input to the collision kernel (see (3.2)) is the relative velocity p.d.f., $P_{ij}(r|w_{ij})$. Unfortunately, statistics from the simulations are not sufficient to obtain $P_{ij}(r|w_{ij})$ directly, hence we define two complementary expectations for negative and positive relative velocities as follows:

$$w_{ij}^{-}(r) = -\int_{-\infty}^{0} w_{ij} P_{ij}(r|w_{ij})\,\mathrm{d}w_{ij}, \tag{3.10}$$

$$w_{ij}^{+}(r) = \int_{0}^{\infty} w_{ij} P_{ij}(r|w_{ij})\,\mathrm{d}w_{ij}, \tag{3.11}$$

where the collision kernel given in (3.2) can be expressed in terms of $w_{ij}^{-}(r)$ as

$$K_{i,j} = 4\pi a_{ij}^2 g_{ij}(a_{ij}) w_{ij}^{-}(a_{ij}). \tag{3.12}$$

We first focus on $w_{ij}^{-}(r)$ since this is the statistic that arises in the collision kernel. Figure 6 shows the evolution of (*a*) $w_{11}^{-}(r)$, (*b*) $w_{22}^{-}(r)$ and (*c*) $w_{12}^{-}(r)$. Included in these graphs are the statistics for interpenetrating ghost particles (dashed line) and particles that undergo a hard-sphere collision without coagulating (solid line). Once again, we see that the relative velocity, much like the r.r.d.f. before (see figure 5*a*), is substantially different from the hard-sphere colliding system, suggesting that the boundary condition modifies this statistic as well. However, coagulation enhances the relative velocity compared to the elastic rebounding case. Indeed, this change may partially compensate for the reduction in the r.r.d.f. shown in figure 5(*a*). We see a similar result for $w_{22}^{-}(r)$, although the scatter in the curve makes it difficult to separate the trend from statistical noise. The curves for $w_{12}^{-}(r)$ are somewhat puzzling since they imply excellent agreement between rebounding and coagulating cases even though both disagree significantly with the ghost particle run.

To gain greater insight into why $w_{11}^{-}(r)$ for the coagulating system differs from the elastic rebound case, it is useful to compare the statistics of inwardly moving particles with those of outwardly moving particles, defined by $w_{11}^{+}(r)$. For the elastic rebound case, all inwardly moving particles that collide produce outwardly moving particles with precisely the same statistics; consequently, $w_{11}^{-}(r)$ and $w_{11}^{+}(r)$ are identical at all separation distances. In contrast, coagulation biases the two directions. Figure 7(*a*) shows $w_{11}^{-}(r/a_{11})$ and $w_{11}^{+}(r/a_{11})$ for a coagulating system. As r/a_{11} approaches unity, the population of outwardly moving particles decreases. The reason is that inwardly moving monomers that collide produce a dimer that is no longer counted. Thus, coagulation imposes a bias that strongly favours inwardly moving particles over outwardly moving particles (see the p.d.f. in figure 7*b*). Furthermore, as r/a_{11} approaches unity, $w_{11}^{+}(r)$ decreases since the population of outwardly moving particles in this limit arises solely from particle pairs undergoing near misses at glancing angles that, by definition, have a vanishingly small radial component. Conversely, inwardly moving particles are biased towards faster moving particles, making $w_{11}^{-}(r)$ larger than it is for the elastic rebound case.

3.4. *Explanation for trends in the particle size distribution*

As noted earlier, there is a large matrix of particle interactions that ultimately control the evolution of the particle size distribution. Nevertheless, by examining a few low-order interactions, it is possible to explain qualitatively the trends observed earlier in the particle size distributions. From the results presented in § 3.2 and § 3.3, we see that over the range of Stokes numbers considered in this study, the effect of the r.d.f. on

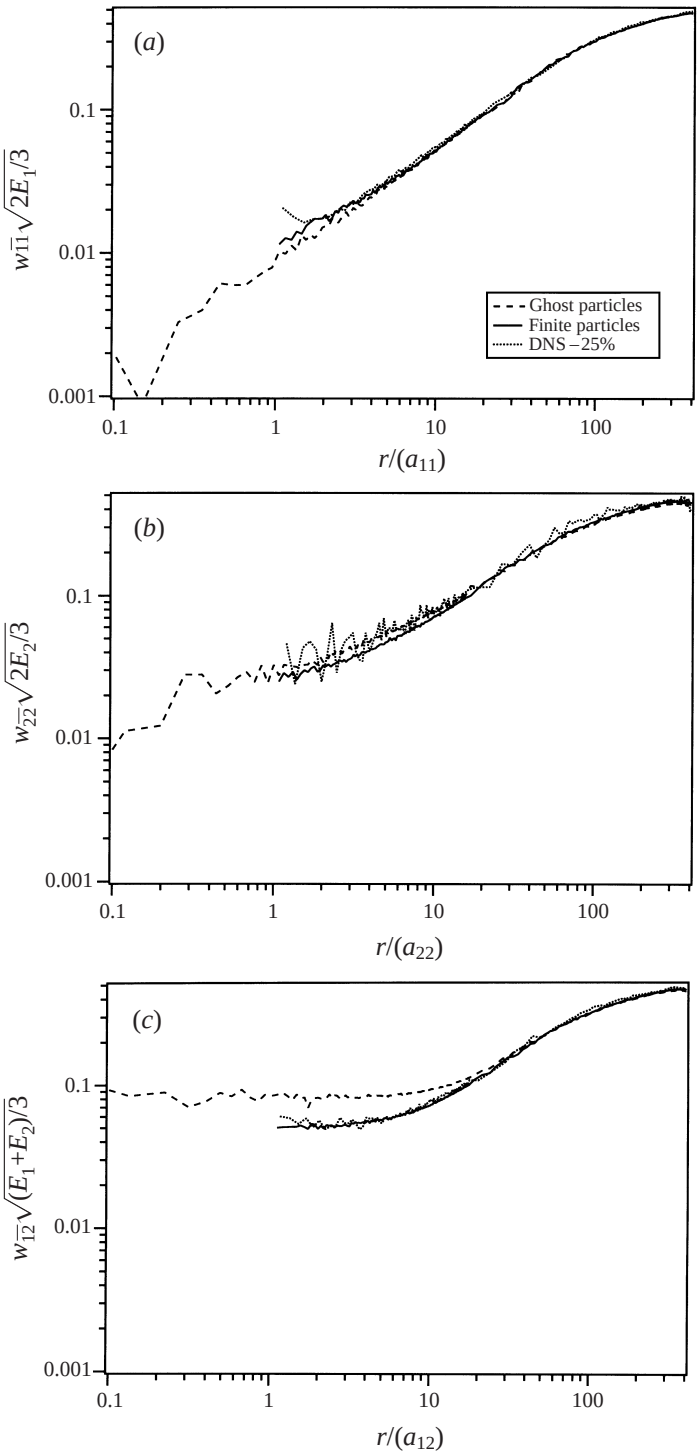

FIGURE 6. Average relative velocities normalized by their respective r.m.s. velocities: (*a*) $w_{11}^{-}/\sqrt{2E_1/3}$, (*b*) $w_{22}^{-}/\sqrt{2E_2/3}$, and (*c*) $w_{12}^{-}/\sqrt{(E_1+E_2)/3}$ for rebounding particles, ghost particles and for coagulating particles at 25% coagulation.

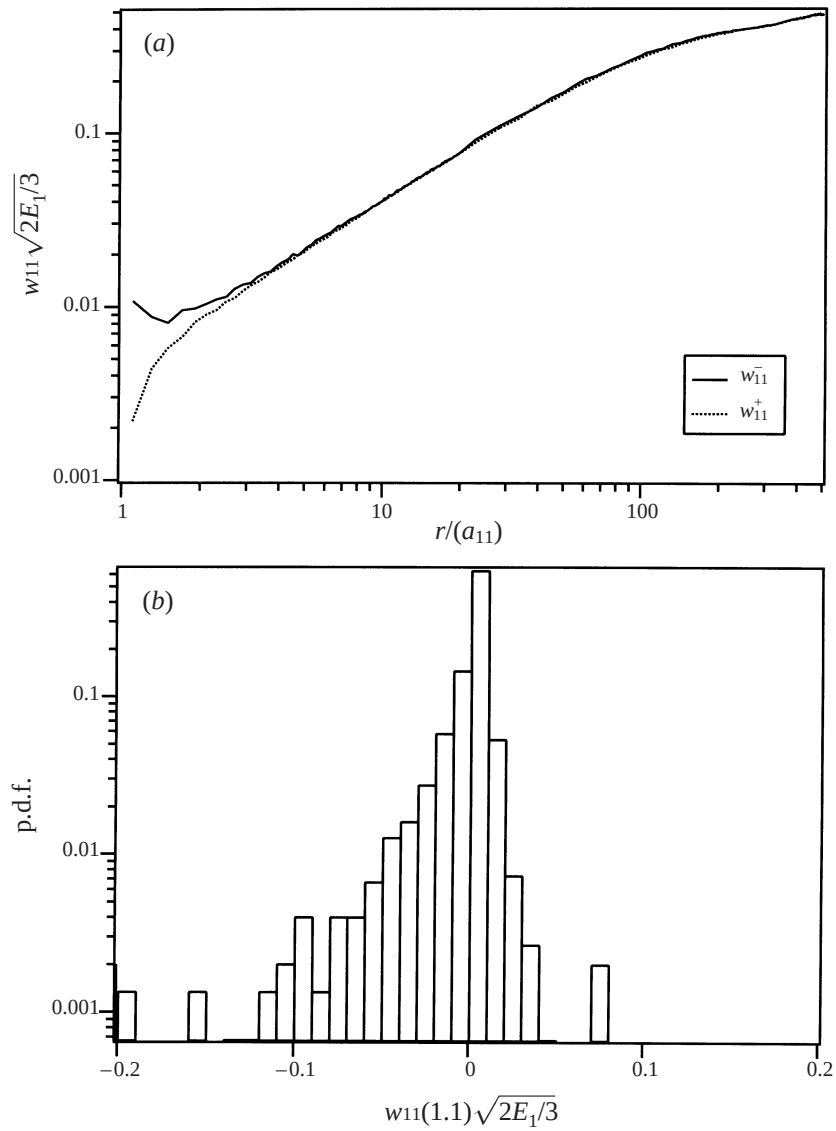

FIGURE 7. (*a*) Relative velocity of inwardly moving particles (w_{11}^-) and outwardly moving particles (w_{11}^+), normalized by the r.m.s. velocity, as a function of separation distance for a coagulating system. (*b*) Probability density function of relative velocities at $r/a_{11} = 1.1$. Here, the break in symmetry associated with coagulation is readily apparent.

the collision kernel is numerically greater than the effect of variations in the relative velocity statistics. Thus, for the sake of simplicity, we focus this discussion on the contribution the r.d.f. makes to the collision kernel. This assumption is reasonable for particles with small-to-moderate Stokes numbers. Furthermore, we limit the discussion to the diagonal r.d.f. terms, i.e. $g_{ii}(a_{ii})$. As noted earlier, off-diagonal terms are generally smaller in magnitude and so have less of an influence on the particle size distribution. Because our goal is only to explain the qualitative trends in the DNS, we feel justified in considering only the dominant contributions to the collision kernel.

First we consider the trend in figure 2 which shows that a smaller initial Stokes

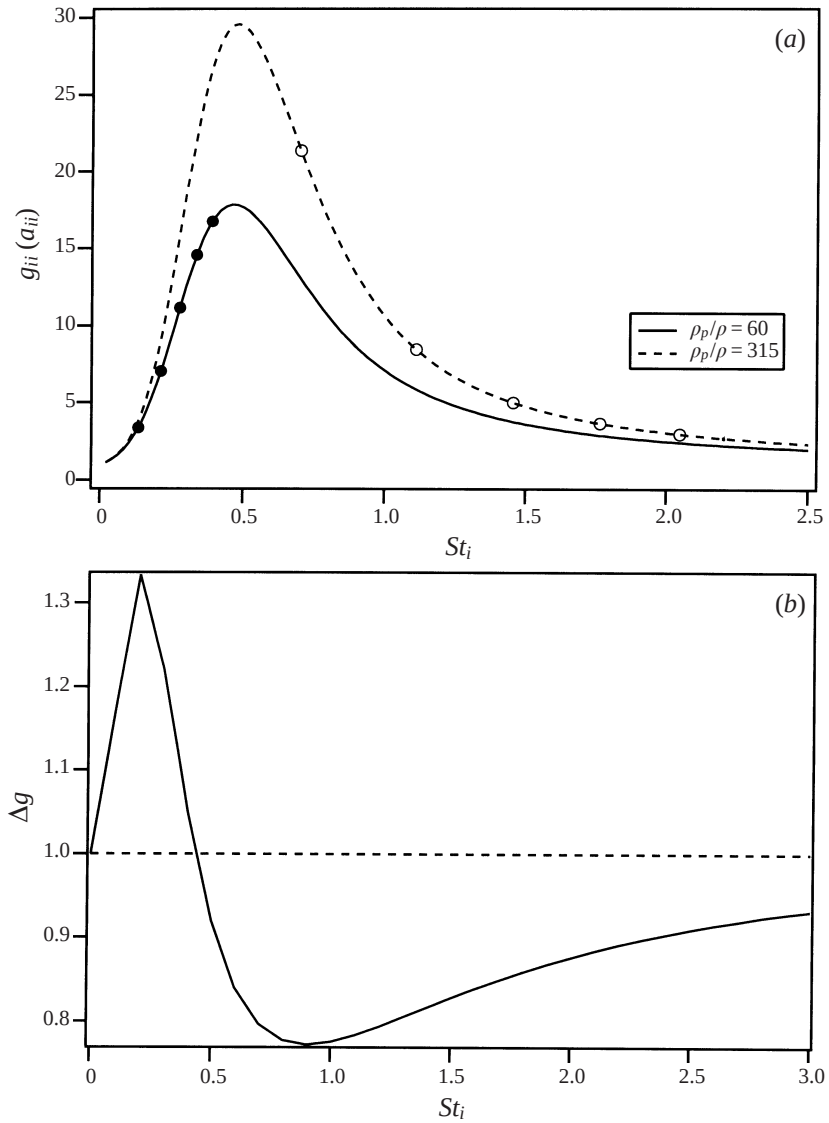

FIGURE 8. (*a*) Collision enhancement factor for like particles with a density ratio $\rho_p/\rho = 60$ and 315 as a function of Stokes number. Solid circles represent a progression of monomer, dimer, trimer, etc. for particles with an initially small Stokes number ($St_1 = 0.1$). Open circles represent the equivalent for a particle with a larger initial Stoke number ($St_1 = 0.7$). (*b*) Δg (see (3.13) for the definition) as a function of the monomer Stokes number.

number leads to a broader distribution. If we define the initial Stokes number of the monomer as St_1, then the Stokes number of any given i-mer is by definition $St_i = i^{2/3}St_1$. Figure 8(*a*) shows the monodisperse r.d.f. for a rebounding system with two particle densities as indicated (taken from the correlations developed by Reade & Collins 2000*a*). Although these curves are not accurate for a coagulating system, the qualitative features remain the same. In particular, notice that the curve reaches a maximum around $St = 0.5$. The circles shown on the graph represent the r.d.f. for a monomer, dimer, trimer, etc. for each curve. Particles starting with a relatively

small Stokes number (solid line and solid circles) have several generations of daughter particles with collision kernels that are enhanced relative to parent particles. The trend continues until the peak in the curve is reached (corresponding to $i = 6$ in this case). This enhancement in the collision kernel resulting from the r.d.f. tends to broaden the distribution. Equivalently, this can be thought of as increasing the effective power, p, in (3.8), thus broadening the distribution. In contrast, particles starting with a larger initial Stokes number (dashed line and open circles) experience a diminished collision kernel for each subsequent generation. This trend slows down the broadening the particle size distribution, or equivalently reduces the effective power p of the collision kernel. Thus, particles with small initial Stokes numbers tend to have broad particle size distributions.

The second set of results shown in figure 4 are somewhat subtler to explain. In particular, understanding how the trend reverses at different initial Stokes numbers requires an understanding of how the r.d.f. depends on both particle size and Stokes number. To facilitate this, we define a variable Δg as follows:

$$\Delta g \equiv \frac{g_{22}(2^{1/3} \times 0.04375, 2^{2/3} \times St_1)/g_{11}(0.04375, St_1)}{g_{22}(2^{1/3} \times 0.175, 2^{2/3} \times St_1)/g_{11}(0.175, St_1)}. \tag{3.13}$$

Δg is effectively a measure of the 'acceleration' in the dimer-collision kernel relative to the monomer-collision kernel for small particles (numerator) compared to large particles (denominator). When Δg is greater than unity, small particles are 'accelerated' faster (i.e. produce a broader size distribution) than large particles. Conversely, when Δg is less than unity, the opposite is true.

As noted earlier, the r.d.f. is a sensitive function of both the Stokes number and the size parameter λ. In particular, the r.d.f. increases with decreasing size parameter at a given Stokes number because smaller particles 'pack' more tightly than larger particles due to their smaller excluded volumes. The effect is captured in the correlation developed by Reade & Collins (2000*a*). Figure 8(*b*) shows Δg as a function of St_1 based on this correlation. Notice that small particles experience a stronger acceleration at low St_1 whereas large particles are favoured at large St_1. This is consistent with the results shown in figure 4 which show broader distributions for small particles at lower St_1 and large particles at higher St_1.

An explanation for the trend in figure 8 can be found by considering the leading-order term in the Reade & Collins (2000*a*) correlation

$$g_{ii}(\lambda_i, St_i) \approx C(St)\lambda^{-p(St)}, \tag{3.14}$$

where $C(St)$ and $p(St)$ are empirical functions that each have a maximum around $St \approx 0.5$. Substituting (3.14) into (3.13) yields

$$\begin{aligned}\Delta g &\approx \frac{C(2^{2/3}St_1)(2^{1/3}0.04375)^{-p(2^{2/3}St_1)}}{C(St_1)(0.04375)^{-p(St_1)}} \times \frac{C(St_1)(0.175)^{-p(St_1)}}{C(2^{2/3}St_1)(2^{1/3}0.175)^{-p(2^{2/3}St_1)}} \\ &= \left(\frac{0.04375}{0.175}\right)^{[p(St_1)-p(2^{2/3}St_1)]}.\end{aligned} \tag{3.15}$$

As $[p(St_1) - p(2^{2/3}St_1)]$ changes sign near $St_1 = 0.5$, Δg changes from being greater than unity for $St_1 < 0.5$ to being less than unity for $St_1 > 0.5$

To summarize, a qualitative understanding of the results reported in § 3.1 has been obtained by considering only a few low-order interactions. Clearly, a first-order analysis such as this cannot be expected to quantitatively explain all of the details

of the particle size distribution since we have neglected off-diagonal contributions to the r.d.f. and have not taken into account relative velocity statistics. Both will probably influence the longer-time behaviour of the size distribution. Nevertheless, a remarkably robust picture emerges from these simple considerations that appears to explain all of the trends observed in the simulations.

4. Conclusions

This paper presented a numerical study of coagulating particles in stationary, isotropic turbulence. The fluid velocity was updated using a standard pseudospectral algorithm and the trajectory of each particle was calculated in a Lagrangian sense. Crossing trajectories lead to coagulation events that produced a daughter particle with the mass and linear momentum of the colliding parents. By following a large population of these particles (initial concentrations of 262 144 particles), it was possible to determine the particle size distribution over time. The study focused on the effect of the initial particle size and Stokes number.

Bounding solutions for the limit of zero or infinite Stokes number proved to be ineffective in describing the evolution of finite-Stokes-number particles. In general, particles with finite Stokes number yielded particle size distributions that were much broader than either of the two limits. Likewise, fitting the collision kernel to a simple algebraic form also proved to be ineffective.

Explanations for the behaviour of the particle size distribution could only be found by examining the two underlying statistics that control the collision kernel, namely the r.d.f. and the relative velocity p.d.f. For particles with relatively small Stokes numbers, the r.d.f. was found to have the greatest influence on the early-time behaviour of the particle size distribution. In particular, preferential concentration leads to a strong enhancement of like-particle collisions and only a modest enhancement of unlike-particle collisions. The combination of effects leads to a broadening of the particle size distribution. By considering the functional dependence of the r.d.f. on the particle size parameter and Stokes number, it was possible to explain the relative trends seen in the particle size distribution. Increasing the particle Stokes number tends to decrease the breadth of the particle size distribution. In contrast, the trend with particle size depends on the Stokes number. At small Stokes numbers, small particles produce the largest variance in the distribution, whereas at large Stokes numbers, small particles produce the smallest variance. The level of analysis presented in § 3.4 may be sufficient to predict trends even in complicated systems. For example, based on the simple arguments presented earlier, one can determine the direction the breadth of a particle size distribution will take given a change in a system parameter such as the local dissipation rate, ϵ.

The above results combined with a more detailed analysis of the r.d.f. suggests that a quantitative model for the collision kernel in a coagulating system must take into account the effect of coagulation on the r.d.f. and the relative velocity p.d.f. Moreover, a dynamic model based on evolution equations is ultimately required to describe the transient nature of the r.d.f.s. Such a model, combined with the population balance given in (3.1), can be used to describe the evolution of the particle size distribution under all conditions.

The authors gratefully acknowledge financial support from the National Science Foundation, Grant CTS-9417527. All computations were performed on IBM SP2 nodes that were provided by generous support from the IBM Shared University Research (SUR) program.

REFERENCES

Abrahamson, J. 1975 Collision rates of small particles in a vigorously turbulent fluid. *Chem. Engng Sci.* **30**, 1371–1379.

Adachi, Y., Stuart, M. A. C. & Fokkink, R. 1994 Kinetics of turbulent coagulation studied by means of end-over-end rotation. *J. Colloid Interface Sci.* **165**, 310–317.

Brunk, B. K., Koch, D. L. & Lion, L. W. 1997 Hydrodynamic pair diffusion in isotropic random velocity fields with application to turbulent coagulation. *Phys. Fluids* **9**, 2670–2691.

Brunk, B. K., Koch, D. L. & Lion, L. W. 1998*a* Turbulent coagulation of colloidal particles. *J. Fluid Mech.* **364**, 81–113.

Brunk, B. K., Koch, D. L. & Lion, L. W. 1998*b* Observations of coagulation in isotropic turbulence. *J. Fluid Mech.* **371**, 81–107.

Canuto, C., Hussaini, M. Y., Quarteroni, A. & Zang, T. A. 1988 *Spectral Methods in Fluid Dynamics*. Springer.

Chen, M., Kontomaris, K. & McLaughlin, J. B. 1998 Direct numerical simulation of droplet collisions in a turbulent channel flow. Part I: collision rates. *Intl J. Multiphase Flow* **24**, 1105–1138.

Eaton, J. K. & Fessler, J. R. 1994 Preferential concentration of particles by turbulence. *Intl J. Multiphase Flow* **20**, 169–209.

Elghobashi, S. 1991 Particle-laden turbulent flows: direct simulation and closure models. *Appl. Sci. Res.* **48**, 301.

Elghobashi, S. E. & Truesdell, G. C. 1992 Direct simulation of a particle dispersion in a decaying isotropic turbulence. *J. Fluid Mech.* **242**, 655–700.

Eswaran, V. & Pope, S. B. 1988 An examination of forcing in direct numerical simulations of turbulence. *Comput. Fluids* **16**, 257–278.

Fairweather, M., Jones, W. P., Ledin, H. S. & Lindstedt, R. P. 1992 Predictions of soot formation in turbulent, non-premixed propane flames. In *Twenty-Second Symp. (Intl) on Combustion*. Combustion Institute.

Kusters, K. A., Wijers, J. G. & Thoenes, D. 1997 Aggregation kinetics of small particles in agitated vessels. *Chem. Engng Sci.* **52**, 107–121.

Maxey, M. R. 1987 The gravitational settling of aerosol particles in homogeneous turbulence and random flow fields. *J. Fluid Mech.* **174**, 441–465.

Maxey, M. R. & Riley, J. J. 1983 Equation of motion for a small rigid sphere in a nonuniform flow. *Phys. Fluids* A **26**, 883–889.

McLaughlin, J. B. 1994 Numerical computation of particles-turbulence interaction. *Intl J. Multiphase Flow* **20**, 211–232.

Moody, E. G. & Collins, L. R. 2000 Effect of mixing on nucleation and growth of titania particles. *Aerosol Sci. Tech.* (submitted).

Pinsky, M. B. & Khain, A. P. 1997 Turbulence effects on droplet growth and size distribution in clouds – a review. *J. Aerosol Sci.* **28**, 1177–1214.

Pratsinis, S. E., Zhu, W. & Vemury, S. 1996 The role of gas mixing in flame synthesis of titania powders. *Powder Tech.* **86**, 87–93.

Reade, W. C. & Collins, L. R. 1998 Collision and coagulation in the infinite-Stokes-number regime. *Aerosol Sci. Tech.* **29**, 493–509.

Reade, W. C. & Collins, L. R. 2000*a* Effect of preferential concentration on turbulent collision rates. *Phys. Fluids* (submitted).

Reade, W. C. & Collins, L. R. 2000*b* On the exceptional broadening of the particle size distribution of aerosol particles in turbulence. *Phys. Rev. Lett.* (in preparation).

Rosner, D. E. & Tassopoulos, M. 1991 Correction for sampling errors due to coagulation and wall loss in laminar and turbulent flow: direct solution of canonical 'inverse' problem for log-normal size distributions. *J. Aerosol Sci.* **22**, 843–867.

Saffman, P. G. & Turner, J. S. 1956 On the collision of drops in turbulent clouds. *J. Fluid Mech.* **1**, 16–30.

Shaw, R. A., Reade, W. C., Collins, L. R. & Verlinde, J. 1998 Preferential concentration of cloud droplets by turbulence: effects on the early evolution of cumulus cloud droplet spectra. *J. Atmos. Sci.* **55**, 1965–1976.

Smoluchowski, M. 1917 Versuch einer mathematischen theorie der koagulationskinetic kolloider losungen. *Z. Phys. Chem.* **92**, 129.

Squires, K. D. & Eaton, J. K. 1991 Preferential concentration of particles by turbulence. *Phys. Fluids* A **3**, 1169.

Sundaram, S. & Collins, L. R. 1996 Numerical considerations in simulating a turbulent suspension of finite-volume particles. *J. Comput. Phys.* **124**, 337–350.

Sundaram, S. & Collins, L. R. 1997 Collision statistics in an isotropic, particle-laden turbulent suspension. Part 1. Direct numerical simulations. *J. Fluid Mech.* **335**, 75–109.

Sundaram, S. & Collins, L. R. 1999 A numerical study of the modulation of isotropic turbulence by suspended particles. *J. Fluid Mech.* **379**, 105–143.

Wang, L. P. & Maxey, M. R. 1993 Settling velocity and concentration distribution of heavy particles in homogeneous isotropic turbulence. *J. Fluid Mech.* **256**, 27–68.

Wang, L.-P., Wexler, A. S. & Zhou, Y. 1998*a* On the collision rate of small particles in isotropic turbulence. 1. zero-inertia case. *Phys. Fluids* **10**, 266–276.

Wang, L.-P., Wexler, A. S. & Zhou, Y. 1998*b* Statistical mechanical descriptions of turbulent coagulation. *Phys. Fluids* **10**, 2647–2651.

Yuu, S. & Umekage, T. 1996 Measurements of turbulent coagulation process in turbulent flow and comparison with calculated results. *JSME* B, **39**, 731–739.

Zhou, Y., Wexler, A. S. & Wang, L.-P. 1998 On the collision rate of small particles in isotropic turbulence. ii. finite-inertia case. *Phys. Fluids* **10**, 1206–1216.